

Human-induced changes to the global ocean water-masses and their time of emergence

Yona Silvy, Éric Guilyardi, Jean-Baptiste Sallée, Paul J. Durack

▶ To cite this version:

Yona Silvy, Éric Guilyardi, Jean-Baptiste Sallée, Paul J. Durack. Human-induced changes to the global ocean water-masses and their time of emergence. Nature Climate Change, 2020, 10.1038/s41558-020-0878-x . hal-02933530

HAL Id: hal-02933530 https://hal.science/hal-02933530

Submitted on 8 Sep 2020

HAL is a multi-disciplinary open access archive for the deposit and dissemination of scientific research documents, whether they are published or not. The documents may come from teaching and research institutions in France or abroad, or from public or private research centers. L'archive ouverte pluridisciplinaire **HAL**, est destinée au dépôt et à la diffusion de documents scientifiques de niveau recherche, publiés ou non, émanant des établissements d'enseignement et de recherche français ou étrangers, des laboratoires publics ou privés.

1	
2	Human-induced changes to the global ocean water-masses
3	and their time of emergence
4	
5	
6	Yona Silvy ^{1,*} , Eric Guilyardi ^{1,2} , Jean-Baptiste Sallée ¹ and Paul J. Durack ³
7	
8	¹ LOCEAN-IPSL, Laboratoire d'Océanographie et du Climat : Expérimentation et
9	Approches Numériques (Sorbonne Université/CNRS/IRD/MNHN), Paris, France
10	² NCAS-Climate, University of Reading, UK
11	³ Program for Climate Model Diagnosis and Intercomparison, Lawrence Livermore
12	National Laboratory, Livermore, California, USA
13	
14	
15	Corresponding author:
16	Yona Silvy (yona.silvy@locean-ipsl.upmc.fr)
17	LOCEAN-IPSL
18	Sorbonne Université, Boîte 100, 4 place Jussieu, 75252 Paris
19	

20 [Abstract]

21 The World Ocean is rapidly changing, with global and regional modification of 22 temperature and salinity, resulting in widespread and irreversible impacts. While 23 the most pronounced observed temperature and salinity changes are located in 24 the upper ocean, changes in water-masses at depth have been identified and will 25 likely strengthen in the future. Here, using 11 climate models, we define when 26 anthropogenic temperature and salinity changes are expected to emerge from 27 natural variability in the ocean interior along density surfaces. The models 28 predict that in 2020, 20-55% of the Atlantic, Pacific and Indian basins have an 29 emergent anthropogenic signal; reaching 40-65% in 2050, and 55-80% in 2080. 30 The well-ventilated Southern Ocean water-masses emerge very rapidly, as early 31 as the 1980s-1990s, while the Northern Hemisphere emerges in the 2010s-2030s. 32 Our results highlight the importance of maintaining and augmenting an ocean 33 observing system capable of detecting and monitoring persistent anthropogenic 34 changes.

35 [Main]

36 Observed ocean temperature and salinity changes have been partially attributed to 37 human activities, with global ocean heat content change identified in the early 2000s^{1,2}, 38 and temperature and salinity changes in the upper (0-700 m) and intermediate (700-2000 m) ocean in more recent times³⁻¹¹. A few studies focused on more specific 39 40 regions, with detected human-induced changes to ocean salinity in the Tropical 41 Pacific⁹, the Atlantic¹⁰, and the Southern Ocean¹¹. However, there are still vast regions 42 of the World Ocean, particularly at depth, where anthropogenic change remains 43 undetected. The lack of positive attribution can be due to poor observational coverage, 44 weak changes, or because natural variability is large and is hiding forced changes. 45 Because of the slow transport of heat and salt in the ocean interior, some regions in the 46 deep ocean may be isolated from human-induced changes for a long time as the climate 47 signal propagates from the surface to the ocean interior. Other regions, which are more 48 directly connected to the surface by atmosphere-ocean exchanges, ocean circulation 49 and mixing, may respond more quickly. Based on anthropogenically-forced climate 50 model simulations it is possible to estimate where and when the human-induced signal 51 emerges against the natural background climate variability in the ocean interior.

52

While investigating the timescale of anthropogenic signal emergence in the climate system, past studies have focused on surface temperature^{12–17}, precipitation^{18,19}, sea level rise²⁰ as well as marine ecosystem drivers and ocean carbon cycle indicators^{21– ²⁶. It was shown that temperature and salinity are potentially good indicators for detecting anthropogenic change in the next few decades²⁷. Here, we investigate for the first time the emergence and associated probabilistic range of human-induced salinity changes at depth, in basin-scale zonal means, using a multi-model framework. We}

60 focus on the ocean interior below the "bowl", i.e. below the deepest winter mixed layer 61 and we use climate models participating in the 5th phase of the coupled model 62 intercomparison project (CMIP5). Ocean circulation below the bowl primarily flows 63 along density surfaces. Density surfaces can move vertically (heave) for several 64 reasons including transient dynamical changes unrelated to atmosphere-forced and 65 ocean-ingested heat or freshwater changes, that manifest as temperature and salinity 66 changes when assessed on a given pressure level. In an endeavour to detect the earliest 67 time of emergence, we therefore remove from our analysis all signal associated to 68 transient dynamical change by investigating temperature and salinity changes on 69 neutral density levels (see Methods). On a density surface, changes of salinity and 70 temperature are by definition correlated, so to avoid redundancy we will hereafter only 71 discuss salinity changes.

72

73 Observed zonally-averaged salinity changes along density surfaces show remarkably 74 similar structures across different basins in the Southern Hemisphere (Figure 1a, 75 Supplementary Figure $(1a)^{28,29}$. These features include a subtropical freshening in the 76 upper 1000 metres in the density range of Subantarctic Mode and Intermediate Waters (26.5-27 kg.m⁻³), surrounded by a relatively strong salinity increase in the tropical 77 shallow cells and a slightly more moderate salinity increase in the range of Upper 78 79 Circumpolar Deep Waters (~50°S-60°S, ~27.5 kg.m⁻³). The Northern Hemisphere 80 Pacific presents a similar geographical salinification/freshening/salinification pattern 81 of change. The North Atlantic features a subpolar freshening extending into the subtropics along the 27.7-28 kg.m⁻³ isopycnals as well as a freshening along the 27 82 kg.m⁻³ isopycnal from the subtropics to the equator and southward, capped by a strong 83 84 salinity increase in the upper ocean and smaller increase at depth. Strong salinification

is observed in the North Indian, spanning almost all density ranges and suggesting theinfluence of marginal sea outflows of high salinity dominates.

These large-scale patterns of multi-decadal change have been proposed to be caused by regional surface changes in freshwater fluxes^{29–32} (wet regions get wetter and dry regions get dryer), as well as from surface warming shifting isopycnal outcrops poleward and along which the signal penetrates the ocean interior^{30–32}.

91

92 Although the amplitude of the change is weaker in the multi-model mean (MMM of 93 11 models; Figure 1b and Supplementary Figure 1b) than in the observation-based 94 estimate – which is expected for a multi-model ensemble mean as it washes out change 95 patterns of water-masses with slightly different geographies thus not exactly aligned -96 reproduced. the main patterns of change are Indeed, the observed 97 salinification/freshening/salinification from equator to pole in the Southern 98 Hemisphere of all three basins and in the Northern Hemisphere Pacific is replicated in 99 the models, although we note the Mode Water freshening in the Southern Hemisphere 100 tends to appear on slightly lighter density classes in the models than in the observations 101 (around 26 kg.m⁻³ in the models versus 26.5-27 kg.m⁻³ in the observations), consistent with past studies^{11,31,33}. The magnitude of change within the individual model 102 103 ensembles is equivalent to observed estimates (Supplementary Figure 3) and the 104 change is robust across models in regions where the observed signal is the strongest, 105 indicative of a coherent forced change. The Northern Indian ocean shows a change 106 pattern of opposite sign in the MMM than in observations, as models have large 107 regional errors there. As the Durack & Wijffels 2010 (hereafter DW10) analysis ends 108 in 2008 (Figure 1a), we also compute the 1950-2017 change using the $EN4^{34}$ 109 observation-based ocean reanalysis (Supplementary Figure 2a). The EN4 spatial

patterns of change are extremely similar to those of DW10, giving confidence in the robustness of these identified observed patterns. In the MMM, the patterns of change identified during the 1950-2008 period (Figure 1b and Supplementary Figure 1b) become more robust when extending the period to 2017 and the amplitude of the change increases (Supplementary Figure 2b).

115 To more quantitatively compare the observed and simulated trends in water-masses 116 regionally, a diagnostic of the trends in 9 regions of interest is shown (Figure 1c). In 117 both observations and models, these regions correspond to the salinity increase in the 118 subpolar Southern Ocean, the freshening in the Southern Hemisphere subtropics, the 119 increase (freshening) in the northern subtropical Atlantic (Pacific) and the increase in 120 the subpolar North Pacific. The coordinates are chosen to best capture these patterns 121 and tailored to the water-mass ranges of each model as those are not necessarily 122 reproduced at the same locations. Approximate boxes are shown in Figure 1a, and the 123 exact boxes can be found in Supplementary Figure 1a for the observations and 124 Supplementary Figure 4 for each model. We also run the same diagnostic for EN4. 125 Regional trends in the observational estimates and models (Figure 1c) are within the 126 same order of magnitude, although the DW10 values tend to lie systematically on the 127 higher end of the model distribution or even outside in some sections of the poorly-128 sampled Southern Hemisphere, suggesting that the models might simulate a 129 conservative estimate of the change. In the well-sampled Northern Hemisphere, both 130 observational estimates fall within the model distribution. In all regions, EN4 yields a 131 smaller trend than DW10, consistent with the respective methods of these estimates 132 (in data-sparse regions, EN4 is restored towards the climatology, thus providing a very 133 conservative estimate of change). Overall, this gives us confidence in the ability of 134 models to reproduce these regional patterns of change.

136 Based on the same model suite, we now determine the "anthropogenic" component of 137 the change by subtracting from the salinity computed in the historical simulations, the 138 salinity computed in idealized coincident simulations where human-induced forcings are removed (historicalNat). At the end of the 20th century it is striking that the 139 140 simulated historical change (Figure 1b) is very close to the estimated "anthropogenic" 141 contribution (Figure 2a), with a Pearson's spatial correlation coefficient of 0.88, 142 suggesting that human-induced forcings are responsible for most of the observed salinity change during the 2nd half of the 20th century^{5,9–11}. The pattern of the historical 143 144 anthropogenic signal is further amplified from 2006 and into the 21st century under a 145 high emission scenario (RCP8.5; Figure 2b), confirming the robustness of the 146 structures of the anthropogenic forced change over the observed time period. As this 147 signal appears qualitatively robust and human-induced, we now investigate when it 148 can be statistically unambiguously distinguished from natural background variability 149 over the 1861-2100 period (note that unlike previous studies, we use "natural" rather 150 than "unforced" variability, see Methods).

151

152 We define the time of emergence (ToE) of salinity change as the year when the 153 anthropogenic signal (ranging from 1861 to 2100) exceeds and never falls back below 154 twice the typical natural variability "noise" threshold (the interannual standard 155 deviation of the historicalNat experiment), such that emergence is detected within the 156 95% confidence interval (see Methods for details). We are choosing a rather high 157 estimate of the noise envelope (see Methods), thus possibly yielding conservative ToE 158 results. Nevertheless, early detection is found: in all regions that show a robust pattern of change, the multi-model median ToE falls between the late 20th century and the first 159

160 decades of the 21st century (Figure 3a) and there is a noteworthy agreement between 161 models on the sign of the signal (see also inter-model spread in Supplementary Figure 162 5). Regions that do not emerge show no agreement between models (grey areas in 163 Figure 3a). In 2020, most of the identified forced patterns have already emerged in the 164 ocean interior, with 20-45% of the zonally averaged basin emerged in the Atlantic; 20-55% in the Pacific and 25-50% in the Indian (Figure 3b, 1st-3rd quartiles). These 165 166 numbers rapidly increase, reaching 35-55% in the Atlantic in 2050 to 55-65% in 2080; 167 45-65% to 60-75% in the Pacific; 45-65% to 60-80% in the Indian.

168

169 The earliest ToE are found in the Southern Hemisphere subtropical (40-20°S) and 170 subpolar (60-40°S) areas, with a median ToE as early as the 1980s, and overall earlier 171 than 2020. The subtropical Southern Ocean is a dominant region for heat uptake 172 associated with the formation and subduction of water-masses ventilating the 173 subtropical gyres with Mode and Intermediate waters^{33,35}. The early emergence of the 174 human-induced signal in this region is consistent with the observed changes that have been detected and attributed to anthropogenic forcings¹¹. Model agreement in the 175 176 southern subtropical Atlantic from 40–20°S is weak in the upper 1000 m, reflecting 177 that unlike the Indian and Pacific, this basin is not associated with a well ventilated layer of Subantarctic Mode water³⁵. Instead, the upper 1000 m in the Southern Ocean 178 179 Atlantic basin is populated with newly ventilated Intermediate waters³⁵, whose 180 circulation and subduction are poorly represented by the CMIP5 model suite³³. The 181 model spread is relatively narrow for the Southern Hemisphere subtropics (2-3 decades 182 for the interquartile range in the Pacific and Indian sectors; Supplementary Figure 5), 183 and slightly larger for the subpolar Southern Ocean. We note that the emergence in the 184 subpolar Southern Ocean is to be assessed cautiously, with most models rapidly

limiting spurious open ocean deep convection due to near-surface freshening^{36,37}, 185 186 therefore arguably warming at depth (1000-2000 m) much faster than in the real world 187 (in the subpolar Southern Ocean, deep convection acts to extract heat from the interior 188 ocean and release it to the atmosphere³⁸). The other regions featuring an emergence of the signal in the first decades of the 21st century are the northern Pacific between 10-189 190 30°N and 40°N-60°N, with a median ToE from the 2010s to 2040 and an inter-model 191 range of a few decades. The signal in the North Atlantic also emerges in the early 192 decades of the 21st century, mostly before 2020, with an interguartile range of two to 193 four decades. The inter-model range gives a measure of the uncertainty that the climate 194 models are providing, and so a spectrum of possibilities for the real world to lie within. 195 There is decadal to multi-decadal variability between realizations and between models, 196 as well as model errors, which means it is difficult to get that range below O(10 years). 197

198 Because each model can represent a given water-mass at slightly different latitude or 199 density, we again delineate model-specific water-mass ranges that are uniquely 200 defined for each model, so a clearer, quantitative water-mass centric model 201 intercomparison can be performed (same regions as Figure 1c; see approximate 202 regions in Figure 2b and exact boxes for each model in Supplementary Figure 4 in 203 original density space). Additionally, and again to increase the signal to noise ratio, 204 because each model can have a different climate sensitivity for a given forcing 205 scenario, here we associate, for each model member, the ToE of the anthropogenic 206 signal in all 9 regions to the corresponding global mean surface warming at that time 207 under the RCP8.5 scenario (global mean surface air temperature (GSAT) increase 208 relative to the pre-industrial era, Figure 4). Supplementary Figure 6 shows the same 209 analysis, as a function of time (ToE axis instead of GSAT anomaly).

210 Most models predict that salinity change signals emerge between +0.5°C and +2°C of global mean surface warming, corresponding to a ToE between the late 20th century 211 212 and the first decades of the 21st century (Figure 4). According to this distribution, there 213 is a 100% probability for the anthropogenic signal in the Northern subpolar Pacific and 214 in the Southern Hemisphere Pacific and Indian subtropics to emerge before a +2°C 215 warming, and over 75% probability to emerge before $+1.5^{\circ}$ C – and even before $+1^{\circ}$ C 216 for the Pacific southern subtropics (note observed global mean surface warming to 217 2018 is about 1°C³⁹). The subpolar Southern Ocean sectors have a relatively early 218 median emergence (~0.8°C-1.3°C), but a wide model spread, especially in the Pacific, probably reflecting model deficiencies in representing this part of the ocean 36,37 . The 219 220 Northern Hemisphere subtropical water-masses emerge slightly later than their Southern Hemisphere counterparts (except in the Atlantic basin), with about 75% 221 222 probability to emerge before +2.25°C. We expect the dependence of these results to 223 slower warming scenarios (different RCPs) to be limited, as most models present a 224 signal emerging before there is a significant difference between scenarios (see 225 comparison of the RCP4.5 and RCP8.5 warming in Supplementary Figure 7).

226

227 We repeat the same analysis on an idealized emission scenario where CO2 228 concentration in the atmosphere increases by 1% every year (1pctCO2), i.e. a much faster forcing than observed in the 20th century or projected for the 21st century (see 229 230 Supplementary Figures 6 and 8, and CO2 signal patterns in Supplementary Figure 9). 231 The overall agreement in the emergence of a climate signal in different water-masses 232 across the different models and the two types of very different timing of forcing 233 scenarios (RCP8.5, 1pctCO2) offers confidence in simulated emergence patterns and 234 confirms the dominant role of CO2 emissions.

235

In analysing emergence timescales in the climate system, previous studies^{20,21} showed 236 237 that spatial patterns of ToE are strongly determined by the unforced variability, 238 meaning that an earlier ToE arises in regions of weaker noise and vice-versa. We 239 investigate whether this is the case by examining the relative contributions of signal 240 and noise to the ToE regional pattern for each model, as well as the regional inter-241 model spread (see Supplementary Discussion and Supplementary Figures 12 and 13). 242 We find that the time-independent noise level is not sufficient to explain the ToE 243 spread, which seems predominantly explained by the signal across regions and models, 244 i.e. either its strength, or its decadal to multi-decadal variability. This suggests that the 245 low noise level of the ocean interior makes it a unique place for early detection of 246 human-induced changes, even with the conservative estimate used here. Indeed, 247 although the anthropogenic climate signal might appear at the surface first, strong 248 background variability there can delay its emergence and counter-intuitively earlier 249 emergence can be found in the ocean interior, with geographical differences compared 250 to the surface. Surface air temperature and sea surface temperature in the RCP8.5 251 scenario were found to emerge mainly within the early to mid 21st century, showing 252 strong regional differences with earlier emergence in the tropics due to the low noise level there than at higher latitudes^{14,15,20}. ToE is especially late in the Southern Ocean 253 254 for surface temperature, whereas we find the earliest emergence in this part of the 255 world under the surface. Half of the ocean area is expected to have emergent 256 thermosteric sea level rise in the 2040s, and when including additional effects such as ice mass loss, as early as 2020^{20} . It is interesting to see that the timing of emergence 257 258 of changing patterns occurs differently for different variables, probably a testimony of 259 their distinctive interactions and feedbacks in the Earth system. This is clearly illustrated by the very different patterns and timing of emergence of the change in the
different components of the ocean carbon cycle²⁶. The diversity of climate variables
investigated collectively provides a comprehensive understanding of the time of
emergence of the human-induced change in the Earth System, into which this study is
contributing additional insight.

265

266 This work suggests that a large portion of the observed change patterns in the ocean 267 interior is human-induced and will continue to respond to CO2 emissions. If these 268 patterns have been suggested to be primarily driven by an increased surface warming and water-cycle amplification^{29,31} (two processes that directly affect heat and salt in 269 270 the ocean thus density and circulation), understanding how these patterns will continue to amplify in the future in a more stratified upper ocean⁴⁰ and with possibly modified 271 272 ocean circulation and mixing requires further investigation. In particular deciphering 273 which of the changing surface fluxes is likely to play a larger role, where and on what 274 timescales, can be for example explored with model-specific FAFMIP-like^{41,42} 275 mechanistic studies.

276 The Hemispheric asymmetry in emergence, with earlier ToEs in the Southern 277 Hemisphere subtropics is reminiscent of a number of recent studies stressing the 278 importance of the Southern Ocean for ocean heat and carbon storage, associated with 279 the overturning circulation 43-45. It is noteworthy that this part of the world is 280 historically the most poorly sampled, and therefore the worst positioned for detecting 281 a forced climate signal in observations^{46,47}. The global pattern of human-induced 282 fingerprint of ocean interior change can be used to guide the future development of a 283 targeted global ocean observing system focused at monitoring and detecting future 284 ocean change. The maintenance of this observing system along with continued

investment in climate and ocean model development and evaluation, will provide the
necessary measurements and model tools to best inform adaptation and mitigation
strategies and policies going forward.

288

289

290 [Methods]

291 Density binning of CMIP5 simulations

292 In this study, we use a suite of CMIP5 climate models binned into a neutral density framework, using the McDougall and Jackett (2005)⁴⁸ routine, to examine 293 294 anthropogenic signal in the ocean on approximated neutral surfaces (γ^a) compared with 295 natural climate variability. Zonal means are computed for each oceanic basin along 296 neutral density surfaces, which allows for a more water mass-centric assessment than 297 is possible using a standard pressure level analysis. We note that some vertical 298 movement (heave) of density surfaces can be due to climate change^{49,50}, but we don't 299 investigate those here. In addition to providing a cleaner signal and reducing the noise, 300 the density framework provides several other benefits, including a view of the ocean interior delineated by its water-masses, useful for intermodel comparison^{33,51}, as water-301 302 masses can be defined by their density range. Additionally, along density surfaces, 303 salinity and temperature changes compensate and thus have the same structure and 304 sign, and consequently the same emergence timescale.

To allow for a simpler and more intuitive visual representation, zonally-averaged values are then remapped back to a pseudo-depth coordinate using a γ^a to pressure relationship derived from observation-based product EN4³⁴ by a surface-to-bottom mapping of the ocean per density layer. Note that all remapping of this paper, irrespective of whether we are in the context of past, contemporary, or future, is done

with the exact same γ^{a} to pressure relationship which is based on contemporary observations. The remapping is purely a visual tool here, which does not introduce any signal: all signal, noise and ToE computations are done in γ^{a} space. All the data is trimmed at the bowl (i.e. below the winter mixed layer depth), indicated by a dark grey shading in the figures.

315

316 **ToE definition**

The ToE is computed both locally (for each grid point; Figure 3) and regionally in a 317 318 number of determined regions, using a manual fingerprint (i.e. regional model-specific 319 boxes fixed in time) to track the signal (Figure 4). We use an ensemble of 11 models 320 with a total of 35 realizations for the anthropogenic ToE, and 13 single-member 321 models for the CO₂ ToE (see Supplementary Table 1). The ToE is computed for each 322 individual member, then inter-member medians are derived, yielding a multi-model distribution with the same weight for each model, and thus an estimate of the 323 324 uncertainty.

325 The anthropogenic signal is 240 years long, ranging from 1861 to 2100. It is defined 326 over the historical period (1861-2005) at each yearly time step as the salinity difference 327 between the historical experiment (fully-forced) and the time averaged historicalNat 328 value (natural forcings only: solar fluctuations and volcanic eruptions); and defined 329 over the projection period (2006-2100) at each yearly time step by the salinity change 330 between the RCP8.5 scenario ("business as usual") and the time averaged historicalNat 331 value (same baseline for both periods to insure continuity). For each 332 historical+RCP8.5 ensemble member, the historicalNat time series used as the baseline 333 of the signal is the ensemble mean.

We note that the correct term for the signal defined above should be "externally forced" as the influence of external natural forcings can be present during the historical period; however, considering the greater influence of human-induced forcings over time and especially in the ocean interior, we therefore refer to this signal as "anthropogenic". The possible influence of external natural forcings in the signal during the historical period will occur in terms of additional decadal to multidecadal variability.

341 The noise represents the bounds of background climate variability, and is built from 342 the interannual standard deviation of the historicalNat experiment (1861-2005, over 343 145 years). Within several historical+RCP8.5 members of a model, the noise is the 344 same and is defined using the maximum standard deviation of all available 345 historicalNat realizations within that model. The threshold of signal exceedance over 346 noise is chosen at two based on the large consensus in existing literature, and because 347 it represents a 95% confidence of signal emergence, but sensitivity to this threshold is 348 discussed in the Supplementary Materials (see Supplementary Figure 10). Overall, this 349 definition makes it a rather high (thus conservative) estimate of the noise envelope 350 (interannual noise, historicalNat choice instead of a pre-industrial control, two 351 standard deviations as the threshold and picking the maximum among historicalNat 352 members). The signal is considered to have emerged if it definitively exceeds the noise 353 threshold at least 20 years before the end of the projection to account for potential 354 "false" emergence - i.e. if the signal were to go back within the bounds of climate 355 variability afterwards^{20,52}. Note that some internal variability (and natural variability 356 over the historical period due to volcanic and sun forcings) remains in our signal 357 definition, which is not exactly the purely forced response to anthropogenic forcings

358 such as can be identified with the multi-model mean of a large ensemble, but is rather 359 a change and thus more similar to what real observational time series would look like. 360 The historicalNat experiment is a coherent choice for estimating natural climate 361 variability as it accounts for internal variability as well as external natural forcings, 362 both included in the forced experiments. However, we do test how our results are 363 affected by using the pre-industrial control (no external forcings) instead of the 364 historicalNat experiment in defining the noise, as is often done, and do not find the 365 time of emergence distributions to be much altered (see Supplementary Figure 11). 366 The change driven by the CO2 forcing alone can be estimated in a similar way, by 367 taking the salinity difference between the yearly idealized 1pctCO2 experiment (140 368 years) and the mean value of the pre-industrial control. The noise for CO2 ToE is then 369 defined as the standard deviation of the pre-industrial control over the last 240 years 370 (as to have the same noise definition as done in Supplementary Figure 11 for the 371 turquoise boxes).

372

373 **ToE distribution of basin zonal means**

374 The gridpoint-per-gridpoint ToE distribution is calculated based on Lyu et al.'s (2014)²⁰ methodology. A signal is considered to have emerged if its ToE is at least 20 375 376 years earlier than the end of the time series (2080 for the RCP8.5, 120 for the 377 1pctCO2). At each gridpoint, the signal of each model realization can emerge with 378 either a positive (salinity increase) or negative (freshening) change, or not emerge at 379 all and stay within the bounds of climate variability. The distribution can be calculated 380 if at least half of the runs emerge with the same sign of the signal, or at least half of 381 the runs show no emergence, and if the outliers that have a different direction of change 382 are less than 5 (5 for the anthropogenic signal, 1 for the pure CO2). We then compute the distribution by excluding the outliers, first by computing the inter-member medians, then the multi-model distribution using these medians so as to give each model the same weight. If the conditions are not met, the location is labelled as "no agreement". See Lyu et al. (2014) supplementary material for details and examples.

387

388 Manual fingerprint

389 The regional ToEs are calculated by averaging both signal and noise in selected regions 390 (see Figure 2b). Namely, we defined: the Southern Ocean subpolar range, 391 encompassing signal associated with Upper Circumpolar Deep Water (around 40-392 60°S; 27-28 kg.m-3); the Southern Ocean subtropical range, encompassing signal 393 associated with Mode and Intermediate Waters (around 20–40°S; 25-26.5 kg.m-3); the 394 Northern Hemisphere subtropical range, encompassing signal associated with Atlantic 395 and Pacific Mode Waters (around 20-40°N; 25-26 kg.m-3 in the Pacific; 26-27 kg.m-396 3 in the Atlantic), and the Subpolar North Pacific, encompassing signal associated with 397 the North Pacific Intermediate Waters (around 40-60°N; 26-27 kg.m-3). The boxed 398 coordinates are model-specific, and were fixed (in γ^a space) based on the zonally-399 averaged spatial pattern of the signal at the end of the time series (see Supplementary 400 Figure 4). The regional emergence of the signal (Figure 4) is based on a manual 401 fingerprint for each region displayed, thus slightly sensitive to the precise boxes used. 402 The patterns of change that already exist in the historical forced simulations continue to exist in the same locations and enhance in the 21st century simulations, giving us 403 404 confidence in using boxes fixed in time.

405

406

408 Warming scale

Global surface warming at emergence was computed by taking each run's GSAT
(historical+RCP8.5) smoothed with a 10-year running mean, at the time of emergence
in each region. GSAT anomaly is calculated relative to the 1850-1900 period. The
same was done for the 1pctCO2 GSAT (Supplementary Figure 8).

Percentage of basin emergence

We define the percentage of emerged area in basin zonal means and under the surface bowl at each time step by computing the cumulative sum over each basin of the number of grid cells that have emerged before that time step, weighted by the thickness of their respective density layer; and dividing it by the cumulative sum of each grid cell's isopycnal thickness of that same basin zonal mean. The result is given in terms of area as the latitudinal grid is regular with a 1° resolution (all models were interpolated on that same horizontal regular grid). This is done for every model simulation, then the inter-member medians are computed. Shown in Figure 3b are the median, 1st and 3rd quartiles of the multi-model distribution.

433 [Acknowledgments]

We wish to thank Casimir de Lavergne, Alexey Fedorov, Peter Gleckler, Jonathan Gregory, Ed Hawkins, Gurvan Madec, Herlé Mercier, Juliette Mignot, Ben Santer and Laurent Terray for helpful discussions. We acknowledge the support from the "Make Our Planet Great Again" project ARCHANGE (Agence Nationale pour la Recherche project ANR-18-MPGA-0001), from the European Research Council (ERC) under the European Union's Horizon 2020 research and innovation program (grant agreement 637770) and from the Centre National de la Recherche Scientifique. We also acknowledge the CMIP5 modelling groups, the ESGF and IPSL/ESPRI-MOD data distribution systems. The work of PJD was prepared by Lawrence Livermore National Laboratory (LLNL) under Contract DE-AC52-07NA27344 and is a contribution to the U.S. Department of Energy, Office of Science, Climate and Environmental Sciences Division, Regional and Global Modeling and Analysis Program. LLNL Release number: LLNL-JRNL-794900.

458 [References]

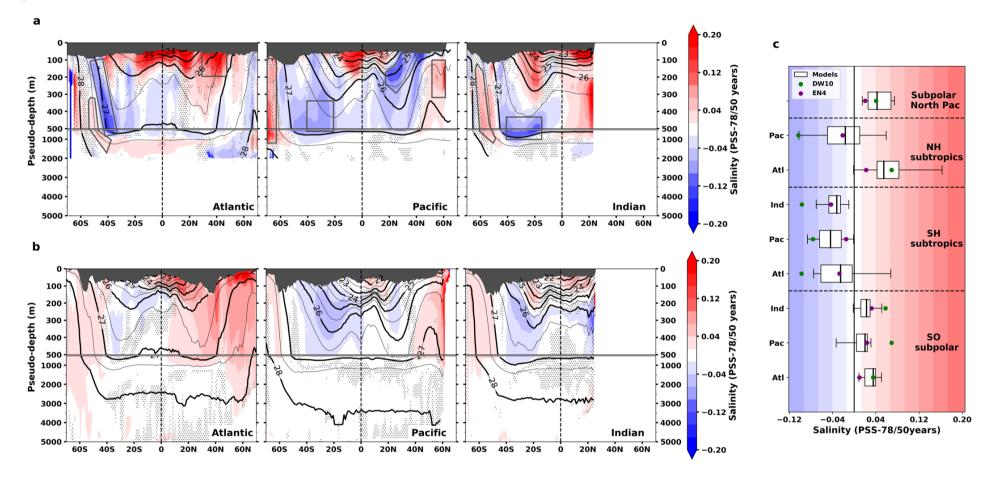
- 459 1. Barnett, T. P., Pierce, D. W. & Schnur, R. Detection of Anthropogenic Climate
 460 Change in the World's Oceans. *Science* 292, 270–274 (2001).
- 461 2. Reichert, B. K., Schnur, R. & Bengtsson, L. Global ocean warming tied to 462 anthropogenic forcing. *Geophys. Res. Lett.* **29**, 20-1-20–4 (2002).
- 3. Barnett, T. P. *et al.* Penetration of Human-Induced Warming into the World's
 Oceans. *Science* 309, 284–287 (2005).
- 465 4. Palmer, M. D., Good, S. A., Haines, K., Rayner, N. A. & Stott, P. A. A new
 466 perspective on warming of the global oceans. *Geophys. Res. Lett.* 36, (2009).
- 467 5. Pierce, D. W., Gleckler, P. J., Barnett, T. P., Santer, B. D. & Durack, P. J. The
- 468 fingerprint of human-induced changes in the ocean's salinity and temperature fields.
- 469 Geophys. Res. Lett. **39**, (2012).
- Gleckler, P. J. *et al.* Human-induced global ocean warming on multidecadal
 timescales. *Nat. Clim. Change* 2, 524–529 (2012).
- 472 7. Tokarska, K. B., Hegerl, G. C., Schurer, A. P., Ribes, A. & Fasullo, J. T.
- 473 Quantifying human contributions to past and future ocean warming and thermosteric sea
 474 level rise. *Environ. Res. Lett.* 14, 074020 (2019).
- 475 8. Bilbao, R. A. F., Gregory, J. M., Bouttes, N., Palmer, M. D. & Stott, P.
- Attribution of ocean temperature change to anthropogenic and natural forcings using the
 temporal, vertical and geographical structure. *Clim. Dyn.* (2019) doi:10.1007/s00382019-04910-1.
- 479 9. Terray, L. *et al.* Near-Surface Salinity as Nature's Rain Gauge to Detect Human
 480 Influence on the Tropical Water Cycle. *J. Clim.* 25, 958–977 (2012).
- 481 10. Stott, P. A., Sutton, R. T. & Smith, D. M. Detection and attribution of Atlantic
 482 salinity changes. *Geophys. Res. Lett.* 35, (2008).
- 483 11. Swart, N. C., Gille, S. T., Fyfe, J. C. & Gillett, N. P. Recent Southern Ocean
 484 warming and freshening driven by greenhouse gas emissions and ozone depletion. *Nat.*485 *Geosci.* 11, 836-+ (2018).
- 486 12. Mahlstein, I., Knutti, R., Solomon, S. & Portmann, R. W. Early onset of
 487 significant local warming in low latitude countries. *Environ. Res. Lett.* 6, 034009
 488 (2011).
- 489 13. Diffenbaugh, N. S. & Scherer, M. Observational and model evidence of global
 490 emergence of permanent, unprecedented heat in the 20th and 21st centuries. *Clim.*

- 491 *Change* **107**, 615–624 (2011).
- 492 14. Hawkins, E. & Sutton, R. Time of emergence of climate signals. *Geophys. Res.*493 *Lett.* 39, n/a-n/a (2012).
- 494 15. Mora, C. *et al.* The projected timing of climate departure from recent variability.
- 495 *Nature* **502**, 183–187 (2013).
- 496 16. Diffenbaugh, N. S. & Charland, A. Probability of emergence of novel
- 497 temperature regimes at different levels of cumulative carbon emissions. *Front. Ecol.*
- 498 *Environ.* **14**, 418–423 (2016).
- 499 17. Lehner, F., Deser, C. & Terray, L. Toward a New Estimate of "Time of
- 500 Emergence" of Anthropogenic Warming: Insights from Dynamical Adjustment and a
- 501 Large Initial-Condition Model Ensemble. J. Clim. 30, 7739–7756 (2017).
- 502 18. Giorgi, F. & Bi, X. Time of emergence (TOE) of GHG-forced precipitation
 503 change hot-spots. *Geophys. Res. Lett.* 36, (2009).
- 504 19. Mahlstein, I., Portmann, R. W., Daniel, J. S., Solomon, S. & Knutti, R.
- 505 Perceptible changes in regional precipitation in a future climate. *Geophys. Res. Lett.* 39,506 (2012).
- 507 20. Lyu, K., Zhang, X., Church, J. A., Slangen, A. B. A. & Hu, J. Time of 508 emergence for regional sea-level change. *Nat. Clim. Change* **4**, (2014).
- 509 21. Keller, K. M., Joos, F. & Raible, C. C. Time of emergence of trends in ocean
- 510 biogeochemistry. *Biogeosciences* **11**, 3647–3659 (2014).
- 511 22. Rodgers, K. B., Lin, J. & Frölicher, T. L. Emergence of multiple ocean
- 512 ecosystem drivers in a large ensemble suite with an Earth system model. *Biogeosciences*
- 513 **12**, 3301–3320 (2015).
- 514 23. Frölicher, T. L., Rodgers, K. B., Stock, C. A. & Cheung, W. W. L. Sources of
- 515 uncertainties in 21st century projections of potential ocean ecosystem stressors. *Glob.*
- 516 Biogeochem. Cycles **30**, 1224–1243 (2016).
- 517 24. Henson, S. A. et al. Rapid emergence of climate change in environmental
- 518 drivers of marine ecosystems. *Nat. Commun.* **8**, 14682 (2017).
- 519 25. Turk, D. et al. Time of Emergence of Surface Ocean Carbon Dioxide Trends in
- 520 the North American Coastal Margins in Support of Ocean Acidification Observing
- 521 System Design. Front. Mar. Sci. 6, (2019).
- 522 26. Schlunegger, S. *et al.* Emergence of anthropogenic signals in the ocean carbon
- 523 cycle. *Nat. Clim. Change* 1–7 (2019) doi:10.1038/s41558-019-0553-2.
- 524 27. Banks, H. & Wood, R. Where to Look for Anthropogenic Climate Change in the

- 525 Ocean. J. Clim. 15, 879–891 (2002).
- 526 28. Helm, K. P., Bindoff, N. L. & Church, J. A. Changes in the global hydrological-527 cycle inferred from ocean salinity. Geophys. Res. Lett. 37, (2010). 528 29. Durack, P. J. & Wijffels, S. E. Fifty-Year Trends in Global Ocean Salinities and 529 Their Relationship to Broad-Scale Warming. J. Clim. 23, 4342–4362 (2010). 530 30. Durack, P. J., Wijffels, S. E. & Matear, R. J. Ocean Salinities Reveal Strong 531 Global Water Cycle Intensification During 1950 to 2000. Science 336, 455–458 (2012). 532 31. Lago, V. et al. Simulating the Role of Surface Forcing on Observed 533 Multidecadal Upper-Ocean Salinity Changes. J. Clim. 29, 5575–5588 (2016). 534 Zika, J. D. et al. Improved estimates of water cycle change from ocean salinity: 32. 535 the key role of ocean warming. Environ. Res. Lett. 13, 074036 (2018). 536 33. Sallee, J.-B. et al. Assessment of Southern Ocean water mass circulation and 537 characteristics in CMIP5 models: Historical bias and forcing response. J. Geophys. 538 Res.-Oceans 118, 1830–1844 (2013). 539 34. Good, S. A., Martin, M. J. & Rayner, N. A. EN4: Quality controlled ocean 540 temperature and salinity profiles and monthly objective analyses with uncertainty 541 estimates: THE EN4 DATA SET. J. Geophys. Res. Oceans 118, 6704–6716 (2013). 542 35. Sallée, J.-B., Speer, K., Rintoul, S. & Wijffels, S. Southern Ocean Thermocline 543 Ventilation. J. Phys. Oceanogr. 40, 509-529 (2010). 544 36. de Lavergne, C., Palter, J. B., Galbraith, E. D., Bernardello, R. & Marinov, I. 545 Cessation of deep convection in the open Southern Ocean under anthropogenic climate 546 change. Nat. Clim. Change 4, 278-282 (2014). 547 37. Heuzé, C., Ridley, J. K., Calvert, D., Stevens, D. P. & Heywood, K. J. 548 Increasing vertical mixing to reduce Southern Ocean deep convection in NEMO3.4. 549 Geosci. Model Dev. 8, 3119–3130 (2015). 550 38. Dufour, C. O. et al. Preconditioning of the Weddell Sea Polynya by the Ocean 551 Mesoscale and Dense Water Overflows. J. Clim. 30, 7719–7737 (2017). 552 39. Intergovernmental Panel on Climate Change. Summary for Policymakers. in 553 Global warming of 1.5°C. An IPCC Special Report on the impacts of global warming of 554 1.5°C above pre-industrial levels and related global greenhouse gas emission 555 pathways, in the context of strengthening the global response to the threat of climate 556 change, sustainable development, and efforts to eradicate poverty (2018). 557 40. Yamaguchi, R. & Suga, T. Trend and Variability in Global Upper-Ocean 558 Stratification Since the 1960s. J. Geophys. Res. Oceans 124, 8933–8948 (2019).

- 559 41. Gregory, J. M. et al. The Flux-Anomaly-Forced Model Intercomparison Project
- 560 (FAFMIP) contribution to CMIP6: investigation of sea-level and ocean climate change
- 561 in response to CO2 forcing. 27 (2016).
- 562 42. Todd, A. *et al.* Ocean-only FAFMIP: Understanding Regional Patterns of Ocean
 563 Heat Content and Dynamic Sea Level Change. (2020).
- 564 43. Gille, S. T. Decadal-Scale Temperature Trends in the Southern Hemisphere
- 565 Ocean. J. Clim. 21, 4749–4765 (2008).
- 566 44. Khatiwala, S. P. et al. Global ocean storage of anthropogenic carbon.
- 567 *Biogeosciences* **10**, 2169–2191 (2013).
- 568 45. Frölicher, T. L. *et al.* Dominance of the Southern Ocean in Anthropogenic
- 569 Carbon and Heat Uptake in CMIP5 Models. J. Clim. 28, 862–886 (2015).
- 570 46. Roemmich, D. *et al.* Unabated planetary warming and its ocean structure since
 571 2006. *Nat. Clim. Change* 5, 240–245 (2015).
- 572 47. Durack, P. J., Gleckler, P. J., Landerer, F. W. & Taylor, K. E. Quantifying
- underestimates of long-term upper-ocean warming. *Nat. Clim. Change* 4, 999–1005
 (2014).
- 575 48. McDougall, T. J. & Jackett, D. R. The material derivative of neutral density. J.
 576 Mar. Res. 63, 159–185 (2005).
- 577 49. Häkkinen, S., Rhines, P. B. & Worthen, D. L. Warming of the Global Ocean:
- 578 Spatial Structure and Water-Mass Trends. J. Clim. 29, 4949–4963 (2016).
- 579 50. Desbruyères, D., McDonagh, E. L., King, B. A. & Thierry, V. Global and Full-
- 580 Depth Ocean Temperature Trends during the Early Twenty-First Century from Argo 581 and Repeat Hydrography. *J. Clim.* **30**, 1985–1997 (2017).
- 582 51. Iudicone, D. *et al.* Water masses as a unifying framework for understanding the
- 583 Southern Ocean Carbon Cycle. *Biogeosciences* **8**, 1031–1052 (2011).
- 584 52. Hawkins, E. et al. Uncertainties in the timing of unprecedented climates. Nature
- 585 **511**, E3–E5 (2014).
- 586

87 [Figures]



88

89 Figure 1 Observed and simulated salinity changes between 1950 and 2008, shown in PSS-78/50 years, analysed on density surfaces. For ease of reading all figures of this paper are projected back from density to pressure as vertical coordinate (see Methods). (a) From Durack & Wijffels (2010) 90 observation-based analysis. Contours show isopycnals and stipples where the trend is not significant at the 90% confidence level. (b) From the multi-model 91 mean historical experiments. Contours show isopycnals and stipples indicate where less than 60% of models agree on the sign of the trend. The changes in 92 93 original density coordinate are shown in Supplementary Figure 1. (c) Trend averaged in 9 regions (approximate boxes shown in panel a) for 2 observational estimates (Durack & Wijffels 2010 - DW10 - and EN4) and for the model distribution (boxes indicate 1st and 3rd guartiles and the median; whiskers indicate 94 95 the minimum and maximum outliers). The shading in (c) corresponds to the colour scale of (a) and (b). The exact regions in density space as used for each observational dataset and model are plotted in Supplementary Figures 1a, 2a and 4 (same coordinates for both observational datasets). The greyed-out regions 96 97 at the surface correspond to data trimming above the bowl - see text.

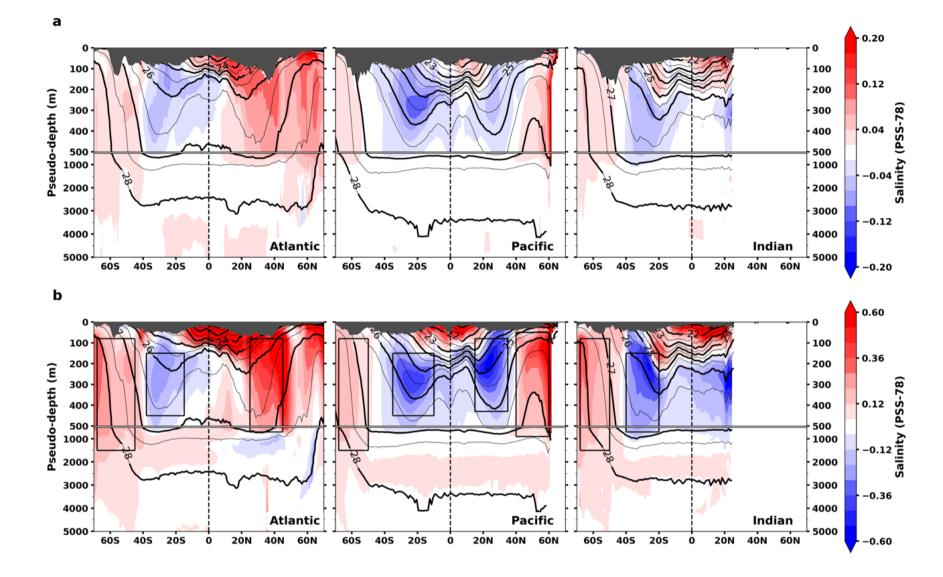


Figure 2 Anthropogenic salinity change along density surfaces. (a) At the end of the 20th century (multi-model mean difference between the last 20 years - to account for potential decadal variability – of the historical experiment and the historicalNat experiment). (b) At the end of the 21st century (multi-model mean difference between the last 20 years of the RCP8.5 scenario and the average of the whole historicalNat experiment). Boxes in (b) represent the approximate regions in which salinity trends are computed in Figure 1c and in which time of emergence is calculated in Figure 4. The same signal as in (b) is shown in Supplementary Figure 4 for each model in density space with the exact box locations.



а

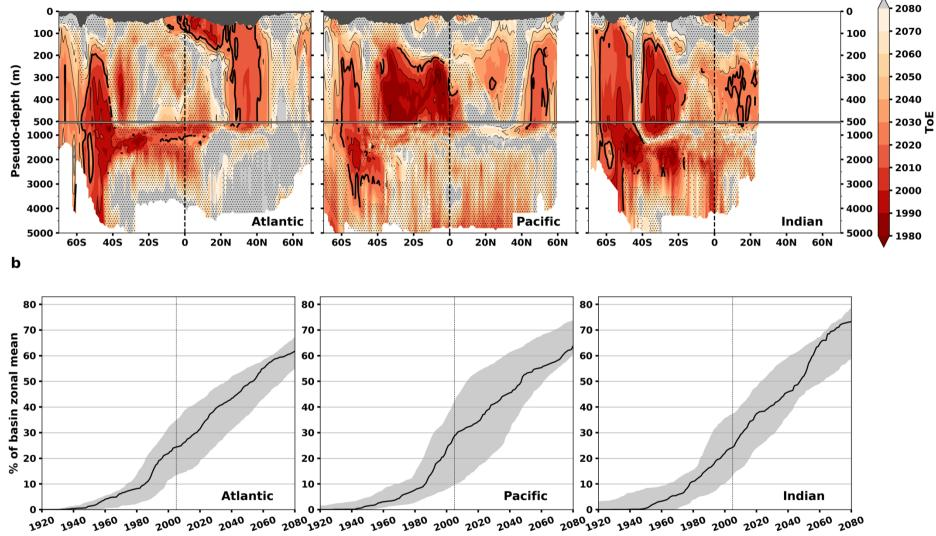
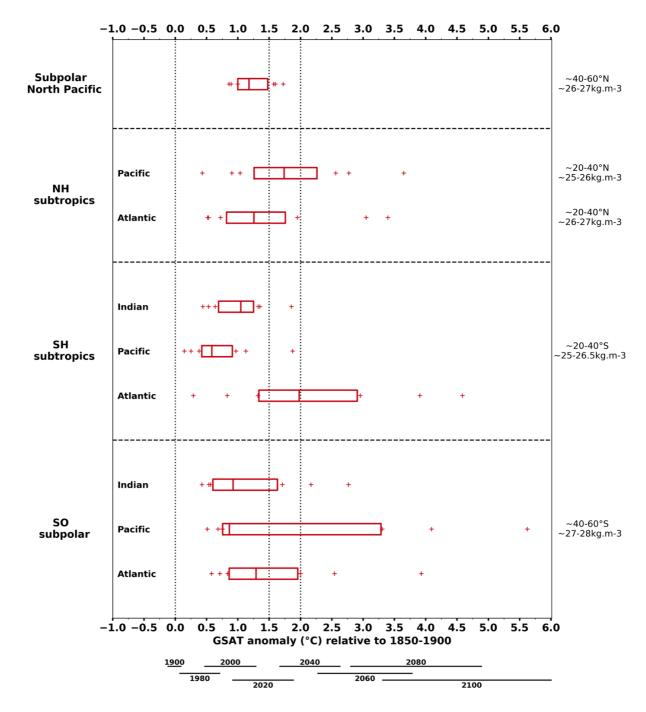


Figure 3 Time of emergence and percentage of emergence in basin zonal-means. (a) Multi-model median time of emergence of the anthropogenic salinity change, calculated for an ensemble of 11 models. Light grey regions mean no emergence of the signal, while stippled regions show where the models don't agree on the sign of the signal (see Methods). Bold contour is year 2020. (b) Percentage of basin emergence in zonal means under the bowl (see Methods). The black line is the median, the grey shading is the interquartile range.



610 Figure 4 Distribution of Global Surface Air Temperature at emergence. 611 Calculated from the anthropogenic salinity signal and noise for each of the 11 612 models in 9 regions of interest: the Southern Ocean subpolar range, the Southern 613 Hemisphere subtropical range, the Northern Hemisphere subtropical range and the 614 subpolar North Pacific (the exact coordinates for each model are shown in Supplementary Figure 4). Red boxes indicate 1st quartile, median and 3rd quartile. 615 A date reference was added below the warming axis, spanning the range of the 616 617 historical and RCP8.5 simulations.